



Cite this: *J. Mater. Chem. A*, 2015, **3**,  
24082

## Hierarchical core–shell heterostructure of porous carbon nanofiber@ZnCo<sub>2</sub>O<sub>4</sub> nanoneedle arrays: advanced binder-free electrodes for all-solid-state supercapacitors†

Hao Niu, Xue Yang, He Jiang, Dan Zhou, Xin Li, Ting Zhang, Jiuyu Liu, Qian Wang\* and Fengyu Qu\*

Hierarchical ZnCo<sub>2</sub>O<sub>4</sub> nanoneedle arrays are vertically grown on porous carbon nanofibers (PCFs) to form a core–shell heterostructure through a facile hydrothermal method followed by thermal treatment. Such a unique configuration makes full use of the synergistic effects from both excellent electrical conductivity of PCFs and high specific capacitance of ZnCo<sub>2</sub>O<sub>4</sub>, endowing the hybrid to be an excellent electrode for flexible supercapacitors. Benefiting from their intriguing structural features, the PCF@ZnCo<sub>2</sub>O<sub>4</sub> hybrid possesses fascinating electrochemical performance as an integrated binder-free electrode for supercapacitors. Remarkably, this PCF@ZnCo<sub>2</sub>O<sub>4</sub> electrode could achieve a high capacitance of 1384 F g<sup>-1</sup> at a scan rate of 2 mV s<sup>-1</sup>. Moreover, an all-solid-state asymmetric supercapacitor fabricated with the as-prepared PCF@ZnCo<sub>2</sub>O<sub>4</sub> hybrid as the positive electrode and PCFs as the negative electrode achieves a high energy density of 49.5 W h kg<sup>-1</sup> (based on the total mass of the material on the two electrodes) at a power density of 222.7 W kg<sup>-1</sup>. Furthermore, the all-solid-state asymmetric supercapacitor device exhibits remarkable cycling stability with 90% specific capacitance retention after 3000 cycles. Therefore, these fascinating electrochemical performances make this material hold great promise for next-generation high-energy supercapacitor applications.

Received 16th September 2015  
Accepted 25th October 2015

DOI: 10.1039/c5ta07439h  
[www.rsc.org/MaterialsA](http://www.rsc.org/MaterialsA)

### 1. Introduction

Nowadays, there has been an ever increasing and urgent demand to seek clean and renewable energy sources because of the increased concerns over environmental pollution caused by conventional energy technologies and the rapid depletion of non-renewable resources.<sup>1–7</sup> Thus, exploiting high-performance energy-related materials for energy storage devices is highly urgent and still remains a major challenge.<sup>8–10</sup> As one of the most promising types of energy storage devices, supercapacitors have attracted tremendous interest as power sources for applications requiring fast bursts of energy or as back-up power sources in electric vehicles owing to their desirable properties such as high power densities,<sup>11,12</sup> fast charge/discharge rates<sup>13</sup> and superior cycling stabilities.<sup>14–18</sup> In general, supercapacitors can be classified into two types based on the underlying energy storage mechanism: electrical double-layer capacitors and pseudocapacitors.<sup>19,20</sup> Pseudocapacitors could make full use of reversible faradic reactions that occur at the surface of an

electrode, offering competitive capacitance compared with electrical double-layer capacitors that store electrical energy in the electric double-layer near the interfaces between electrode and electrolyte.<sup>21</sup>

Pseudocapacitive materials, mainly including transition metal oxides/hydroxides (MnO<sub>2</sub>,<sup>22,23</sup> Co<sub>3</sub>O<sub>4</sub><sup>24</sup> and NiO<sup>25</sup>) and electrically conducting polymers (polyaniline<sup>26</sup> and polypyrrole<sup>27,28</sup>), have been extensively investigated as promising electrode materials for supercapacitors during the past few decades. However, these materials often suffer from low electrical conductivity and serious structural degradation during the cycling process, which significantly deteriorates their power capability at high rates and leads to poor cycling performance, greatly limiting its practical application.<sup>29</sup> Therefore, it is necessary to exploit advanced/novel electrode materials to enhance the energy densities, power capabilities and cycling stabilities to meet the demands of future applications. Considerable research has recently been focused on ternary metal oxides, which could achieve higher specific capacitances than the corresponding single-component metal oxides since they can offer richer redox chemistry and combine the contributions from both metal ions.<sup>30</sup> A series of ternary oxides have been developed as pseudocapacitive electrode materials for supercapacitors, such as NiCo<sub>2</sub>O<sub>4</sub>,<sup>31</sup> MnCo<sub>2</sub>O<sub>4</sub> and CoMn<sub>2</sub>O<sub>4</sub>,<sup>32</sup>

College of Chemistry and Chemical Engineering, Harbin Normal University, Harbin 150025, China. E-mail: wangqianhrb@163.com; qufengyuhsd@163.com; Fax: +86 451 88060653; Tel: +86 451 88060653

† Electronic supplementary information (ESI) available. See DOI: 10.1039/c5ta07439h

and  $\text{ZnCo}_2\text{O}_4$ ,<sup>33,34</sup>  $\text{ZnCo}_2\text{O}_4$ , replacing one cobalt atom by zinc, has been considered an alternative candidate as an electrode material for supercapacitors.<sup>33,34</sup> With a cubic spinel structure, Zn ions occupy the tetrahedral sites and the trivalent Co ions occupy the octahedral sites, revealing brilliant electroactivity over single cobalt oxides.<sup>3</sup> In addition, Zn has other advantages, including low cost, abundant resources, and environmental friendliness. Considering these points, various nanostructured  $\text{ZnCo}_2\text{O}_4$ , such as nanorods,<sup>35</sup> nanowires,<sup>36,37</sup> nanotubes,<sup>37</sup> porous microspheres,<sup>38</sup> nanosheets,<sup>39</sup> and core-shell structures,<sup>33,40</sup> have been intensively investigated as electrode materials for supercapacitors in recent years.

Design and synthesis of advanced electrodes for supercapacitors with excellent electrical conductivity, short ion transport/diffusion path, and direct and intimate contact between active materials and electrolytes without the assistance of a binder are of significant importance to further commercial applications. The core/shell nanofiber arrays with a conductive core are expected to exhibit a robust structure through taking full advantage of the synergistic effects between a highly conductive one-dimensional nanostructure core and electroactive transition metal oxide shell. Therefore, considerable effort has been devoted to synthesizing core/shell nanostructures for high-performance supercapacitors.<sup>41,42</sup>

In this study, we developed the synthesis of unique hierarchical  $\text{ZnCo}_2\text{O}_4$  nanoneedle arrays, vertically grown on porous carbon nanofibers (PCFs), to form core–shell heterostructures through a facile hydrothermal approach followed by heat treatment as binder-free electrodes for electrochemical energy-storage applications. The  $\text{ZnCo}_2\text{O}_4$  nanoneedle arrays are composed of numerous highly crystalline nanoparticles, leaving a large number of mesopores for fast ion transport and effectively alleviating the volume change during the charge/discharge process. The PCF@ $\text{ZnCo}_2\text{O}_4$  hybrid can be straightforwardly used as binder-free electrodes for supercapacitors, exhibiting a high specific capacitance of  $1384 \text{ F g}^{-1}$  at a scan rate of  $2 \text{ mV s}^{-1}$  in  $6 \text{ M KOH}$  aqueous solution. Moreover, a high performance all-solid-state asymmetric supercapacitor (ASC) device with PCF@ $\text{ZnCo}_2\text{O}_4$  as the positive electrode and PCFs as the negative electrode achieves a remarkable energy density of  $49.5 \text{ Wh kg}^{-1}$  at a power density of  $222.7 \text{ W kg}^{-1}$  based on the total material mass of the two electrodes. Moreover, the fabricated ASC device could retain 90% of its initial capacitance after 3000 cycles. This study may pave a promising way to rationally design and fabricate novel  $\text{ZnCo}_2\text{O}_4$ -based nanostructured electrodes free of additives for high-performance energy storage/conversion devices.

## 2. Experimental section

### 2.1. Preparation of phenol-formaldehyde resins

For the preparation of the resin precursor, 0.61 g of phenol was melted at  $42^\circ\text{C}$  and mixed with 0.15 mL of NaOH aqueous solution (20 wt%) under stirring. Then, 1.05 g of formalin (37 wt%) was added into the abovementioned mixture below  $50^\circ\text{C}$ . Furthermore, the mixture was stirred at  $70^\circ\text{C}$  for 1 h, followed by cooling down to room temperature naturally. Subsequently,

the pH value of the system was adjusted to 7 through addition of 0.6 M HCl. Finally, the residual water was removed using rotary evaporation below  $50^\circ\text{C}$ .

### 2.2. Preparation of PCFs

PCFs were prepared through a facile electrospinning method. Typically, 0.5 g of triblock copolymer Pluronic (P123) and 1.4 g of polyvinyl pyrrolidone (PVP) were dissolved in 10 mL of ethanol under vigorous stirring for 1 h. Next, 0.1 mL of 2 M HCl, 3 mL of tetraethyl orthosilicate (TEOS), and 0.4 g of resin precursor were added to form a mixture and stirred for 4 h. Subsequently, the viscous solution was loaded into a 5 mL plastic syringe equipped with a 9-gauge stainless steel nozzle. The solution was electrospun at a voltage of 18 kV. The as-electrospun nanofibers were collected on an aluminum foil and the distance between the nozzle tip and the collector was maintained at 15 cm. The as-collected films were dried at room temperature for 24 h followed by heat treatment in an oven at  $100^\circ\text{C}$  for 24 h. After that, the fibers were carbonized at  $800^\circ\text{C}$  for 4 h under  $\text{N}_2$  with a heating rate of  $2^\circ\text{C min}^{-1}$ . Finally, the silica template was removed with 10 wt% hydrofluoric acid solution and the obtained PCF fabrics were filtered and washed repeatedly with distilled water several times and dried at  $60^\circ\text{C}$  for 12 h.

### 2.3. Preparation of hierarchical PCF@ $\text{ZnCo}_2\text{O}_4$ hybrid

The growth of  $\text{ZnCo}_2\text{O}_4$  nanoneedle arrays on PCFs was achieved through a typical hydrothermal synthesis method combined with a calcination procedure. Typically, 0.01 mol of zinc nitrate hexahydrate ( $\text{Zn}(\text{NO}_3)_2 \cdot 6\text{H}_2\text{O}$ ), 0.02 mol of cobalt nitrate hexahydrate ( $\text{Co}(\text{NO}_3)_2 \cdot 6\text{H}_2\text{O}$ ), 0.05 mol of urea ( $\text{CO}(\text{NH}_2)_2$ ) and 0.02 mol of ammonium fluoride ( $\text{NH}_4\text{F}$ ) were dissolved in 30 mL deionized water under constant magnetic stirring to form a clear red solution. Then, the PCF substrate was immersed into the abovementioned solution and left to stand for 2 h. Afterwards, the abovementioned solution and the PCF substrate were transferred into a 40 mL Teflon-lined stainless steel autoclave, which was sealed and maintained at  $120^\circ\text{C}$  for 5 h in an electric oven. After the autoclave was cooled down to room temperature naturally, the sample was collected, rinsed several times with distilled water and dried in a vacuum oven at  $80^\circ\text{C}$  overnight, followed by annealing at  $400^\circ\text{C}$  in  $\text{N}_2$  atmosphere for 2 h with a heating rate of  $2^\circ\text{C min}^{-1}$  to obtain the PCF@ $\text{ZnCo}_2\text{O}_4$  hybrid. For comparison, a pure  $\text{ZnCo}_2\text{O}_4$  sample was also prepared through the same synthesis procedure without the presence of the PCF substrate.

### 2.4. Material characterizations

The crystallographic structures of the materials were determined by X-ray diffraction (XRD) equipped with Cu K $\alpha$  radiation ( $\lambda = 0.15406 \text{ nm}$ ). X-ray photoelectron spectroscopy (XPS) was characterized using a PHI 5000 ESCA X-ray photoelectron spectrometer with a monochromated Al K $\alpha$  X-ray source (1486.6 eV) to investigate the chemical structure of the materials. The thermal behavior of the materials was analyzed by thermogravimetric analysis (TGA) and differential thermal analysis (DTA,

TG-209) in an air atmosphere. The nitrogen adsorption/desorption, surface areas, and average pore sizes were measured using a Quantachrome NOVA 2000e analyzer. Specific surface areas and pore size distributions were calculated using the Brunauer–Emmett–Teller (BET) and density-functional-theory (DFT) or Barrett–Joyner–Halenda (BJH) models from the adsorption branches, respectively. The microstructure of the samples was investigated by field-emission scanning electron microscopy (SEM, Hitachi S-4800) and transmission electron microscopy (TEM, Tecnai F20).

## 2.5. Electrochemical measurements

All the electrochemical measurements were performed on a CHI 660D electrochemical workstation at room temperature. The working electrodes were fabricated through pressing active material (3.8 mg) between two pieces of Ni foam under 6 MPa. The electrochemical studies of the individual electrodes were carried out with a three-electrode system in 6 M KOH aqueous electrolyte, in which fabricated electrodes, platinum foil and saturated calomel electrode (Hg/HgO) were used as the working, counter and reference electrodes, respectively.

Cyclic voltammetry (CV) tests were done between 0 and 0.45 V (vs. Hg/HgO) at different scan rates. The galvanostatic charge-discharge curves were measured from 3 to 20 A g<sup>-1</sup> within the potential window from 0 to 0.45 V (vs. Hg/HgO) and the electrochemical impedance spectroscopy (EIS) measurements were carried out in the frequency range from 100 kHz to 0.01 Hz at an open circuit potential with an AC amplitude of 5 mV. The specific capacitance of the electrode can be calculated based on the CV curves according to the following equation:

$$C = \int IdV/vmV \quad (1)$$

where  $I$  is the response current density,  $V$  is the potential,  $v$  is the scan rate, and  $m$  is the total mass of the material on the electrodes.

## 2.6. Fabrication of all-solid-state ASC device

The electrochemical performance of the hybrid was further characterized using an all-solid-state ASC device with the prepared PCF@ZnCo<sub>2</sub>O<sub>4</sub> hybrid and PCFs as the positive and negative electrodes, respectively. The polyvinylacetate (PVA)/KOH polymer gel electrolyte was prepared as follows: 4.2 g of PVA and 4.2 g of KOH were mixed in 50 mL of distilled water. The mixture was heated to 85 °C under vigorous stirring until the solution became clear. Subsequently, the electrodes and the cellulose acetate membrane separator were immersed in the PVA/KOH gel for 1 h. After fabrication, the assembled ASC device was dried in a fume hood at room temperature overnight to evaporate the excess water.

The mass ratio of the negative electrode to the positive electrode was decided based on charge balance theory ( $q_+ = q_-$ ). The charge stored ( $q$ ) by each electrode depends on the following equation:

$$q = C \times \Delta V \times m \quad (2)$$

The power density ( $P$ ) and energy density ( $E$ ) of the supercapacitor devices were calculated based on the following equations:

$$E = \frac{1}{2} C \Delta V^2 \quad (3)$$

$$P = \frac{E}{t} \quad (4)$$

where  $C$  is the specific capacitance of the ASC device calculated according to the CV curves based on the total weight of the materials in the two electrodes,  $\Delta V$  is the voltage scan range and  $t$  is the discharge time.

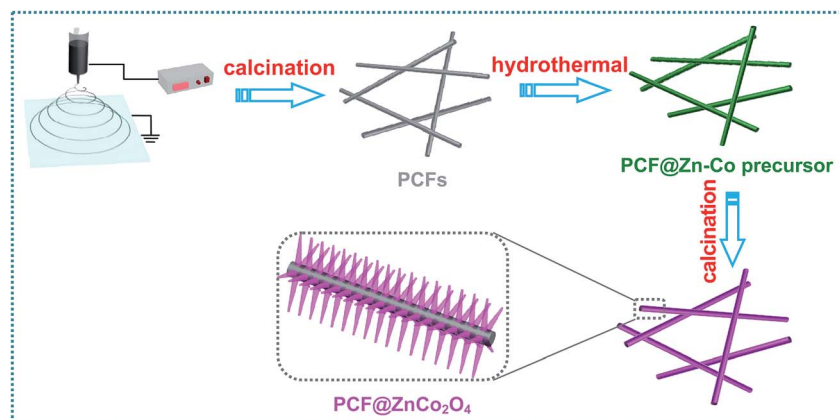
## 3. Results and discussion

### 3.1. Structure and morphology of the PCF@ZnCo<sub>2</sub>O<sub>4</sub> hybrid

The synthetic procedure of PCF@ZnCo<sub>2</sub>O<sub>4</sub> hybrid is illustrated in Scheme 1. First, the PCF substrate is obtained through a facile electrospinning method followed by thermal treatment in an N<sub>2</sub> atmosphere at high temperature. Subsequently, the Zn–Co precursor was successfully grown on the surface of PCF substrate through a hydrothermal reaction. Finally, the as-synthesized PCF@Zn–Co precursor was annealed at 400 °C to allow the Zn–Co precursor to transform into a ZnCo<sub>2</sub>O<sub>4</sub> nanoneedle array to form the hierarchical PCF@ZnCo<sub>2</sub>O<sub>4</sub> heterostructure.

Fig. 1a displays a typical SEM image of the as-prepared PCFs. Obviously, highly uniform carbon nanofibers can be easily obtained through a facile electrospinning method. As is shown, the electrospun nanofibers exhibit relatively smooth surfaces with an average diameter of around 350 nm. In addition, these nanofibers interweave with each other to form a three-dimensional conductive network configuration. From the high magnification TEM image (Fig. 1b), we can see that the PCFs are composed of the graphitic planner structure and considerable micropores and mesopores exist in the carbon fibers, which could be attributed to the decomposition of the polymer and removal of the SiO<sub>2</sub> template.<sup>43,44</sup> Fig. 1c shows the nitrogen adsorption–desorption isotherms of the as-prepared PCFs, which exhibit combined typical I/IV isotherms with an obvious H3 hysteresis loop at relatively low pressure, confirming the existence of micropores in the sample as a result of the decomposition of the polymer.<sup>45,46</sup> The BET specific surface area of the PCFs is calculated to be as high as 1939 m<sup>2</sup> g<sup>-1</sup>. The pore size distribution of PCFs obtained from the adsorption branch of the isotherm is shown in Fig. 1d, indicating that the pore size is mainly in the microporous range (about 1.1 nm and 1.5 nm) and mesoporous range (about 3 nm), which is in good agreement with the TEM image.

The structure and morphology of the as-synthesized hierarchical PCF@ZnCo<sub>2</sub>O<sub>4</sub> hybrid were characterized by SEM. After the hydrothermal reaction and thermal treatment, the smooth surface of PCFs becomes relatively fluffy compared with that of the pristine PCFs. Numerous densely-packed acicular ZnCo<sub>2</sub>O<sub>4</sub> nanoneedle arrays grow uniformly on the skeletons of PCF substrate to form large-scale conformal core–shell



Scheme 1 Schematic of the fabrication of the PCF@ZnCo<sub>2</sub>O<sub>4</sub> hybrid.

nanostructures, as shown in Fig. 2a. The ZnCo<sub>2</sub>O<sub>4</sub> nanoneedle arrays seem like grass growing perpendicular to the surface of the PCF substrate. High-magnification SEM image shown in Fig. 2b clearly depicts that the PCF@ZnCo<sub>2</sub>O<sub>4</sub> hybrid has a uniform diameter of  $\sim 3\text{ }\mu\text{m}$  and the ZnCo<sub>2</sub>O<sub>4</sub> nanoneedle arrays have uniform diameters of 30 nm at the middle section and lengths of about 1.3  $\mu\text{m}$ . It can be noted that each ZnCo<sub>2</sub>O<sub>4</sub> nanoneedle with a rough surface is composed of numerous nanoparticles accumulating with each other to form a highly porous structure due to the release of gaseous species during the calcination process (Fig. 2c). In addition, the meso/macropores among adjacent nanoneedles would facilitate the rapid penetration of the electrolyte ions into the porous structures, which will significantly decrease the transport/migration path

of electrolyte ions during the charge/discharge process. In contrast, without the presence of the PCF substrate, ZnCo<sub>2</sub>O<sub>4</sub> nanoneedles tend to self-assemble into micro-flowers with diameter of approximately 4  $\mu\text{m}$  under same synthetic conditions (Fig. 2d). The crystallographic structure of the material was analyzed by XRD, as shown in Fig. 2e. All the diffraction peaks in the XRD pattern for ZnCo<sub>2</sub>O<sub>4</sub> can be readily indexed to the cubic spinel ZnCo<sub>2</sub>O<sub>4</sub> phase (JCPDS card no. 23-1390; space group: *Fd3m*).<sup>47</sup> With regard to the pristine PCF substrate, the diffraction peaks located at 23.2° and 43.1° can be assigned to the (002) and (100) reflection planes of graphite, respectively.<sup>48</sup> Except for the reflections owing to PCFs, all the other diffraction peaks in the XRD pattern for the PCF@ZnCo<sub>2</sub>O<sub>4</sub> hybrid could be well-ascribed to the spinel ZnCo<sub>2</sub>O<sub>4</sub> phase, definitely

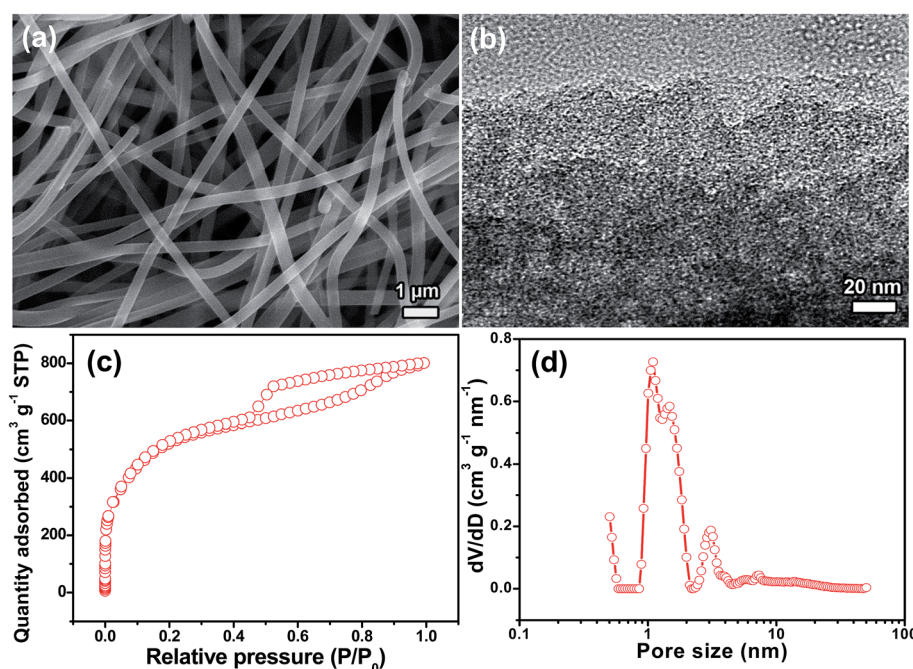


Fig. 1 (a) SEM and (b) high magnification TEM images of the PCFs. (c) Nitrogen adsorption–desorption isotherm and (d) pore size distribution of the PCFs.

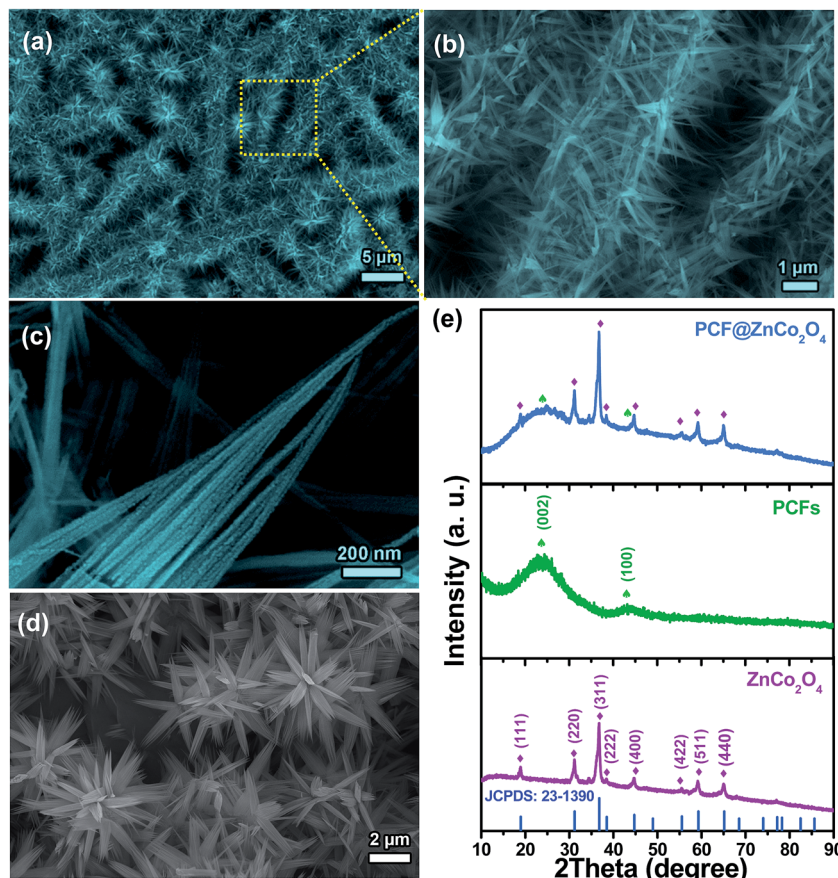


Fig. 2 (a–c) Typical SEM images of the PCF@ZnCo<sub>2</sub>O<sub>4</sub> hybrid. (d) SEM image of pure ZnCo<sub>2</sub>O<sub>4</sub> micro-flowers. (e) XRD patterns of ZnCo<sub>2</sub>O<sub>4</sub>, PCFs and PCF@ZnCo<sub>2</sub>O<sub>4</sub> hybrid.

confirming the successful growth of ZnCo<sub>2</sub>O<sub>4</sub> nanoneedle arrays on the surface of the PCFs.

TEM measurements and selected area electron diffraction (SAED) were carried out to further investigate the detailed microstructure of the as-synthesized PCF@ZnCo<sub>2</sub>O<sub>4</sub> hybrid. As shown in Fig. 3a and b, the ZnCo<sub>2</sub>O<sub>4</sub> nanoneedles are porous and the diameter of the nanoneedles gradually decreases from the root to the tip (~30 nm in diameter at the middle section), which matches well with the abovementioned SEM observation. In addition, the ZnCo<sub>2</sub>O<sub>4</sub> nanoneedles are actually composed of numerous small nanocrystals with the size of about 10 nm instead of the conventional single-crystalline nanoneedle and these nanocrystals interconnect with each other forming a stable porous structure, which is advantageous for electrolyte diffusion and enhances the electrochemical activity.

Nitrogen isothermal adsorption–desorption measurements were performed to determine the porosity and surface area of the materials. Both the nitrogen adsorption–desorption isotherms of the two samples exhibit a typical IV isotherm with a H3-type hysteresis loop, demonstrating the presence of narrow slit-shaped mesopores (Fig. 3c). The BET specific surface area of the PCF@ZnCo<sub>2</sub>O<sub>4</sub> is calculated to be 196 m<sup>2</sup> g<sup>-1</sup>, which is much higher than that of pure ZnCo<sub>2</sub>O<sub>4</sub> (31.7 m<sup>2</sup> g<sup>-1</sup>). The pore size distribution of the ZnCo<sub>2</sub>O<sub>4</sub> calculated from the

adsorption data using the BJH model shows a wide peak centered at 10.3 nm, which further confirms the mesoporous structure of the ZnCo<sub>2</sub>O<sub>4</sub> nanoneedles (Fig. 3d). In contrast, in addition to the mesopores centered at 9.7 nm, considerable micropores with sizes below 2 nm could be clearly found for the PCF@ZnCo<sub>2</sub>O<sub>4</sub> hybrid, which is attributed to the micropores in PCFs substrate. By virtue of its large surface area and porous structure, the PCF@ZnCo<sub>2</sub>O<sub>4</sub> nanoneedle is beneficial in electrical storage applications.

The surface electronic state of the elements and the composition of the PCF@ZnCo<sub>2</sub>O<sub>4</sub> hybrid were analyzed by XPS analysis and the corresponding results are given in Fig. 4. The full-survey-scan spectrum shown in Fig. 4a confirms the presence of Zn, Co and O along with a small quantity of C in the PCF@ZnCo<sub>2</sub>O<sub>4</sub> hybrid. The Zn 2p deconvoluted spectrum exhibits two strong peaks at the binding energy of 1020.9 and 1043.9 eV (Fig. 4b), corresponding to Zn 2p<sub>3/2</sub> and Zn 2p<sub>1/2</sub> levels, respectively, and the spin-energy separation of 23 eV is typical of Zn<sup>2+</sup>.<sup>49</sup> The Co 2p spectrum can also be fitted with two spin-orbit doublets, characteristic of Co<sup>2+</sup> and Co<sup>3+</sup>, and two shake-up satellites (indicated as “Sat”, Fig. 4c).<sup>50,51</sup> The binding energies at around 797.2 and 782.1 eV correspond to Co<sup>2+</sup>, while the binding energies at around 795.4 and 780.1 eV are attributed to Co<sup>3+</sup>. The O 1s spectrum can also be deconvoluted into

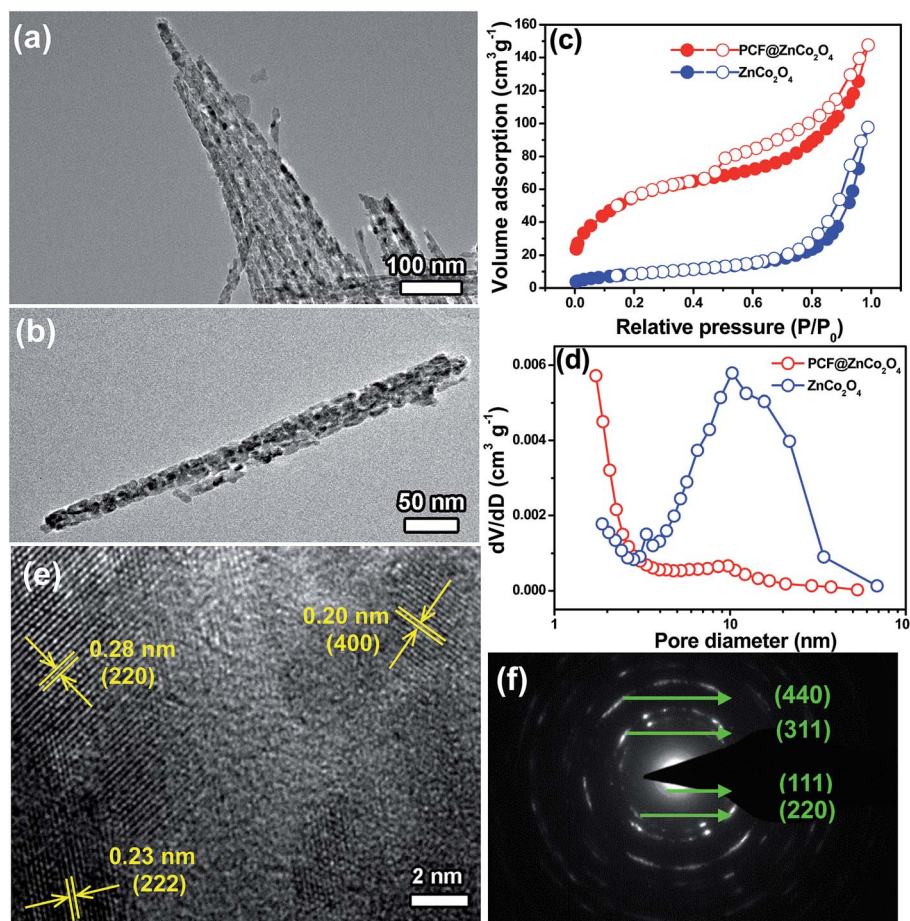


**Fig. 3** (a and b) TEM characterization of  $\text{ZnCo}_2\text{O}_4$  nanoneedles. (c) Nitrogen adsorption–desorption isotherm and (d) pore size distribution of the  $\text{ZnCo}_2\text{O}_4$  and  $\text{PCF}@\text{ZnCo}_2\text{O}_4$  hybrid. (e) High-resolution TEM image of the as-obtained  $\text{ZnCo}_2\text{O}_4$  nanoneedles. (f) Corresponding SAED pattern from an individual nanoneedle.

two components centered at 531 and 529.7 eV (Fig. 4d). The former peak corresponds to the absorption of oxygen and water molecules on the composite surface,<sup>18</sup> while the latter is attributed to the  $\text{O}^{2-}$  forming oxide with Co and Zn elements.<sup>52</sup> Fig. 4e demonstrates the deconvolution of the C 1s spectrum with different oxygen containing functional groups, which can be assigned to non-oxygenated C in C–C at 284.5 eV, carbon in C–O at 286.4 eV, and carbon in C=O at 288.8 eV.<sup>53</sup> Based on the obtained XPS data, the content of  $\text{ZnCo}_2\text{O}_4$  in the hybrid is estimated to be 69.2 wt%. TGA was carried out to further determine the weight percentage of  $\text{ZnCo}_2\text{O}_4$  in the hybrid. TGA and DTA profiles for  $\text{PCF}@\text{ZnCo}_2\text{O}_4$  hybrid are plotted in Fig. 4f. The sample undergoes a weight loss of 32.5 wt% in the temperature range between room temperature to 700 °C with a heating rate of 5 °C min<sup>-1</sup>. The weight loss (3.8 wt%) below 300 °C is assigned to evaporation of moisture and the adsorbed water. The following significant weight loss (28.7 wt%) between 300 °C and 700 °C is assigned to the decomposition of PCFs. Thus, the mass loading of  $\text{ZnCo}_2\text{O}_4$  in the  $\text{PCF}@\text{ZnCo}_2\text{O}_4$  hybrid could be estimated to be about 67.5 wt% from the TGA curve.

### 3.2. Electrochemical characterization of $\text{PCF}@\text{ZnCo}_2\text{O}_4$ hybrid

The electrochemical properties of the  $\text{PCF}@\text{ZnCo}_2\text{O}_4$  hybrid were first examined by CV and galvanostatic discharge–charge measurements with a three-electrode device in 6 M KOH aqueous electrolyte. Fig. 5a shows the CV curves of the pure  $\text{ZnCo}_2\text{O}_4$  and  $\text{PCF}@\text{ZnCo}_2\text{O}_4$  electrodes at a scan rate of 2 mV s<sup>-1</sup>. Noticeably, the CV curve of the  $\text{PCF}@\text{ZnCo}_2\text{O}_4$  hybrid electrode possesses a much larger integrated area than that of  $\text{ZnCo}_2\text{O}_4$  and  $\text{PCF}@\text{Co}_3\text{O}_4$  (Fig. S1†), implying that the  $\text{PCF}@\text{ZnCo}_2\text{O}_4$  hybrid possesses a much higher specific capacitance at the same scan rate. Fig. 5b shows the typical CV curves of the  $\text{PCF}@\text{ZnCo}_2\text{O}_4$  hybrid electrode within the potential range from 0 to 0.45 V (vs. Hg/HgO) at various scan rates. The shape for all of the CV curves seriously deviate from the ideal rectangular shape, which is indicative of an electric double layer capacitor, and all the CV curves exhibit a pair of well-defined redox peaks, indicating that the capacitance is mainly attributed to pseudocapacitance rather than an electric double layer capacitance due to faradic redox reactions. In particular, a pair of strong redox peaks occurring around 0.14/0.24 V (vs. Hg/HgO) can be clearly observed in the scan rate from

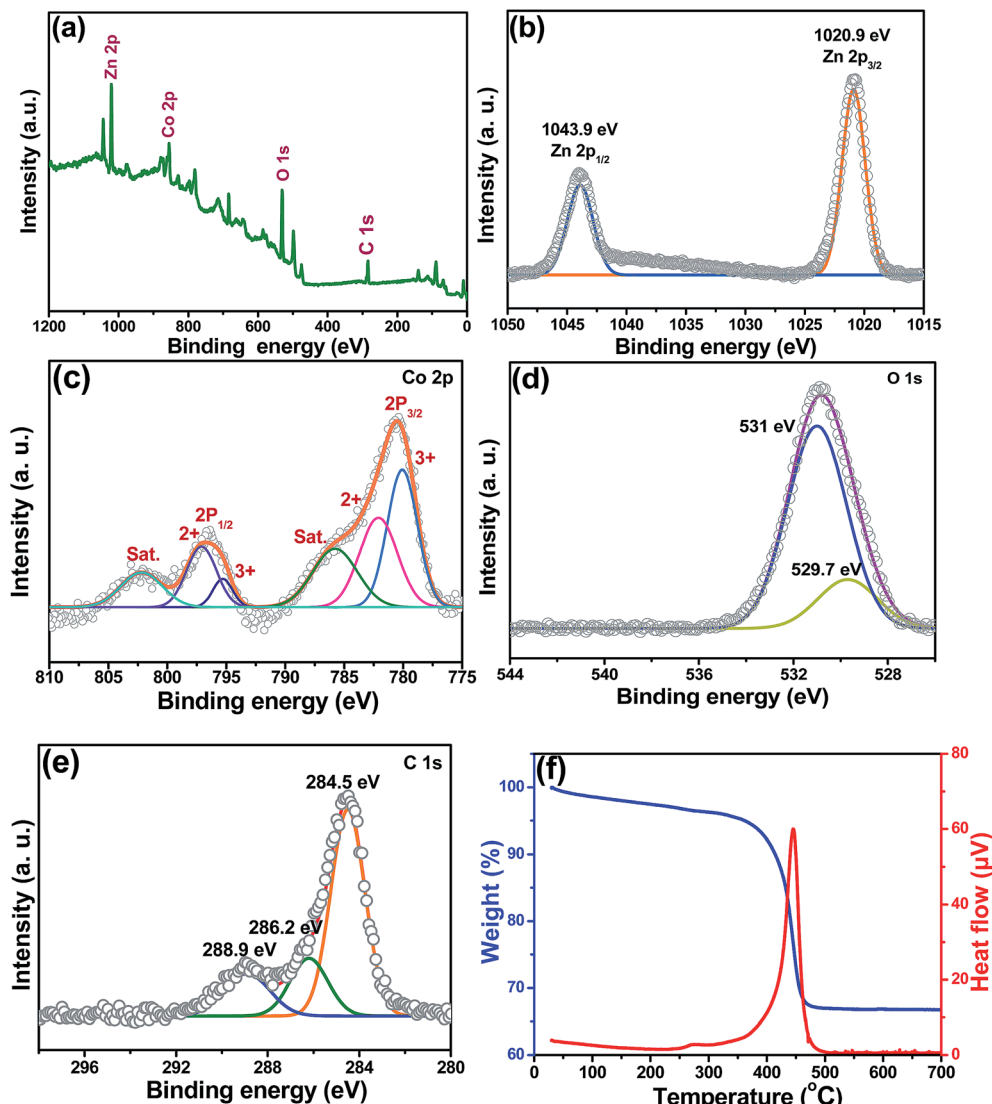


Fig. 4 (a) XPS survey spectrum of PCF@ZnCo<sub>2</sub>O<sub>4</sub> hybrid. (b–e) XPS deconvoluted scans of (b) Zn 2p, (c) Co 2p, (d) O 1s and (e) C 1s. (f) TGA and DTA curves of the as-prepared PCF@ZnCo<sub>2</sub>O<sub>4</sub> hybrid.

2 to 50 mV s<sup>-1</sup>, which is mainly associated with faradic redox reactions related to Co–O/Co–O–OH as in the following equations.<sup>30,54,55</sup>



In addition, the current densities of the redox peaks almost increases linearly with the increase in scan rates, demonstrating excellent kinetics for interfacial faradic redox reactions and the rapid transport of electrons and ions. Moreover, upon the increase of the scan rate from 2 to 50 mV s<sup>-1</sup>, the shape of these CV curves shows no obvious change, implying the excellent rate capability of the hierarchical core–shell array nanostructure. Notably, the anodic and cathodic peaks slightly shift towards higher and lower potential with increasing scan rates,

respectively, which could be attributed to the internal resistance and polarization effect of the electrode. To explain the charge storage mechanism, the relationship between the anodic/cathodic peak current ( $I_p$ ) and the square root of the corresponding scan rate ( $v^{1/2}$ ) is shown in the inset of Fig. 5b. Notably, the anodic and cathodic current increases linearly with the  $v^{1/2}$  at all scan rates, indicating that the redox reaction is a diffusion-controlled process.<sup>53,56,57</sup>

Fig. 5c shows the galvanostatic charge–discharge curves to further pledge the application potential of the as-synthesized hybrid structure as an electrode at different current densities (3, 5, 10, 15 and 20 A g<sup>-1</sup>) in the potential window of 0–0.45 V (vs. Hg/HgO). The charge/discharge curves depict a quintessential deviation from a straight and flat line, which is consistent with the CV curves, demonstrating that the capacitance mainly stems from faradic pseudocapacitance. It could be clearly found that the galvanostatic discharge curves consist of two regions: 0.25–

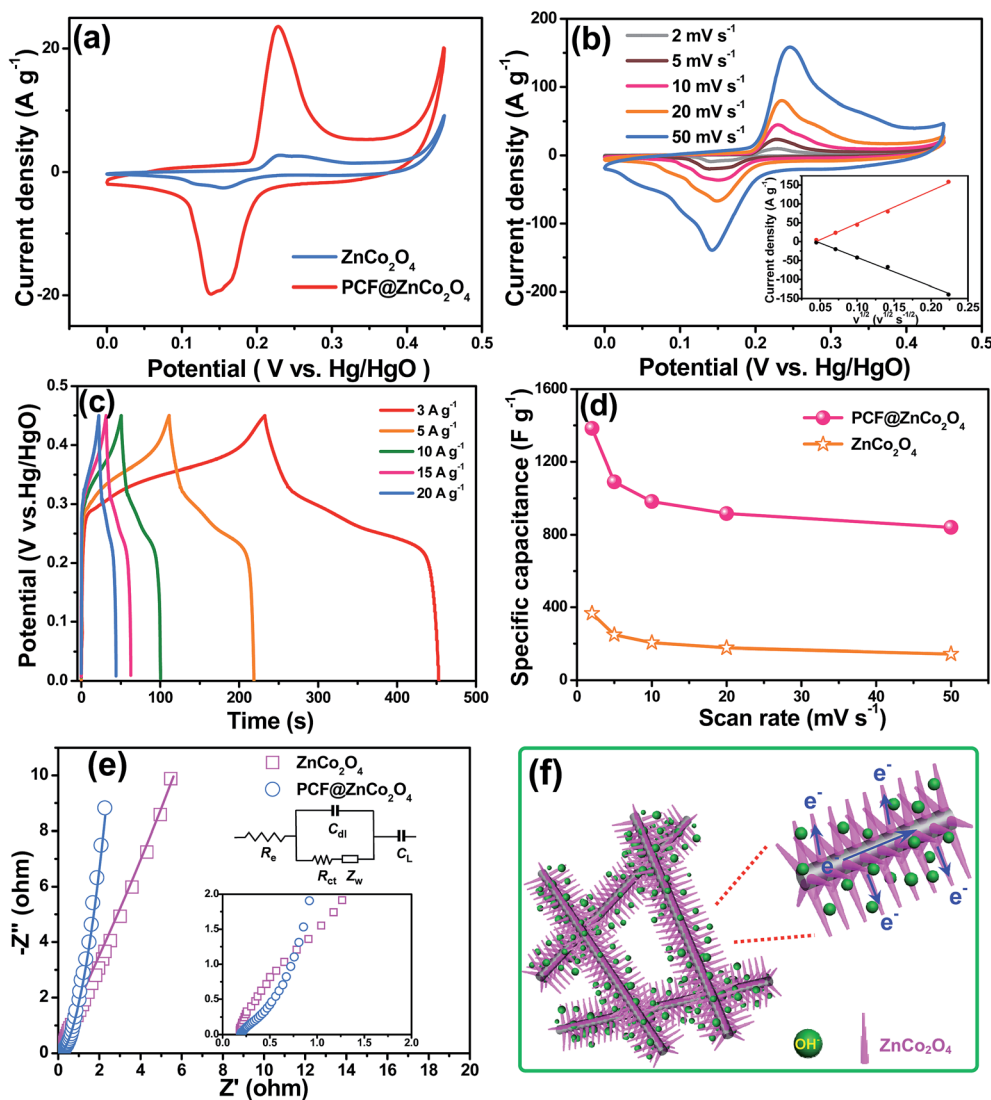


**Fig. 5** (a) CV curves of the ZnCo<sub>2</sub>O<sub>4</sub> and PCF@ZnCo<sub>2</sub>O<sub>4</sub> electrodes at a scan rate of 2 mV s<sup>-1</sup>. (b) CV curves of the PCF@ZnCo<sub>2</sub>O<sub>4</sub> hybrid electrode at various scan rates ranging from 2 to 50 mV s<sup>-1</sup> (inset is the relationship between the peak currents and the square root of the corresponding scan rates in the CV curves). (c) Galvanostatic charge–discharge curves of the PCF@ZnCo<sub>2</sub>O<sub>4</sub> electrode at different current densities. (d) Specific capacitance calculated from CV curves as a function of scan rate. (e) Nyquist plots of the experimental impedance data (scattering dot) and fitting results (solid line) measured at an open circuit potential in the frequency range from 100 kHz to 0.01 Hz. Insets: the electrical equivalent circuit used for fitting impedance spectra and the high-frequency region. (f) Schematic of the charge storage mechanism of the PCF@ZnCo<sub>2</sub>O<sub>4</sub> hybrid.

0.45 and 0–0.25 V (vs. Hg/HgO). In the former region, the potential varies quickly against time so the discharge duration is quite short as a consequence of pure electric double-layer capacitance from the charge separation on the electrode/electrolyte interface. On the other hand, in the latter region, the potential changes slowly against the time with much longer discharge duration, indicating that the capacitance predominately originates from pseudocapacitance due to electrochemical adsorption or rapid redox reaction on the interface between electrode and electrolyte. The specific capacitances are calculated to be 1471, 1196, 1111, 1040, 973 F g<sup>-1</sup> at various current densities. The specific capacitance of the ZnCo<sub>2</sub>O<sub>4</sub> and PCF@ZnCo<sub>2</sub>O<sub>4</sub> electrodes can be calculated from the CV curves

according to eqn (1) and the calculated specific capacitance as a function of scan rate is plotted in Fig. 5d. The PCF@ZnCo<sub>2</sub>O<sub>4</sub> hybrid electrode exhibits a high specific capacitance of 1384 F g<sup>-1</sup> at 2 mV s<sup>-1</sup>, which is much higher than that of the ZnCo<sub>2</sub>O<sub>4</sub> electrode (367 F g<sup>-1</sup>) and the PCF@Co<sub>3</sub>O<sub>4</sub> electrode (267 F g<sup>-1</sup>, Fig. S1a†) at the same scan rate. Although the specific capacitance decreases gradually with the increase in scan rate, a high value of 841 F g<sup>-1</sup> can still be maintained even at 50 mV s<sup>-1</sup> for the PCF@ZnCo<sub>2</sub>O<sub>4</sub> hybrid electrode with a retention ratio of 61%, much higher than that of the pure ZnCo<sub>2</sub>O<sub>4</sub> (39.3%) and PCF@Co<sub>3</sub>O<sub>4</sub> (14.3%) (Fig. S1b†) electrodes. This phenomenon may be explained as follows: Zn ions occupy the tetrahedral sites in the cubic spinel structure and the trivalent Co ions

occupy the octahedral sites. It is well-known that zinc compounds have high electrical conductivity and could act as conductive highways for charge accumulation and transfer of electrons.<sup>49</sup> During the electrochemical process, zinc can improve the electrical conductivity and offer rich redox chemistry, giving rise to further improvements of the overall performance of the electrode material.<sup>34</sup>

Fig. 5e illustrates the electrochemical impedance spectroscopy (EIS) measurements performed on the  $\text{ZnCo}_2\text{O}_4$  and PCF@ $\text{ZnCo}_2\text{O}_4$  hybrid electrode at a frequency range from 100 kHz to 0.01 Hz with a perturbation-potential amplitude of 5 mV. In the high frequency region, there is no distinct semi-circle in the high-to-medium frequency region for the Nyquist plot of the PCF@ $\text{ZnCo}_2\text{O}_4$  hybrid as compared with the  $\text{ZnCo}_2\text{O}_4$  electrode, suggesting high ionic conductivity and fast electron transfer kinetics for redox reactions at the electrode interface.<sup>33,58</sup> In the low frequency region, the slope of the curves shows Warburg resistance, which represents the ion diffusion of electrolyte to the electrode surface. Compared with the  $\text{ZnCo}_2\text{O}_4$  electrode, the PCF@ $\text{ZnCo}_2\text{O}_4$  hybrid electrode presents a more vertical straight line along the imaginary axis, suggesting a much lower

diffusion resistance. This can be attributed to the highly porous structure with large surface areas, which enable enhanced electrolyte penetration and ion diffusion in the host materials. More detailed analysis was carried out using the complex nonlinear least-squares (CNLS) fitting method. The Nyquist plots fit well to the equivalent circuit as shown in the inset of Fig. 5e.  $R_s$  is the series solution resistance, which may include the electrolyte resistance and the active material/current collector contact resistance.  $C_{dl}$  represent double-layer capacitance,  $R_{ct}$  is the charge transfer resistance at the electrode/solution interface,  $Z_w$  is the ion diffusion controlled Warburg impedance, and  $C_L$  is the limit pseudocapacitance.<sup>40</sup> Table 1 shows obtained values of  $R_s$ ,  $C_{dl}$ ,  $R_{ct}$ ,  $Z_w$  and  $C_L$  calculated from CNLS fitting of the experimental impedance spectra. The  $R_s$  and  $R_{ct}$  of the  $\text{ZnCo}_2\text{O}_4$  electrode are 0.227 and 0.547  $\Omega$ , while those of PCF@ $\text{ZnCo}_2\text{O}_4$  electrode are 0.197 and 0.075  $\Omega$ , respectively, indicating a well-connected interface nature of electrolyte ions and electrode after the introduction of the conductive PCF substrate.

The superior electrochemical performance of the PCF@ $\text{ZnCo}_2\text{O}_4$  electrode could be attributed to the following aspects, as shown in Fig. 5f. First, the PCFs serve as substrates, which provide a large surface area ( $1939 \text{ m}^2 \text{ g}^{-1}$ ) for the growth of the  $\text{ZnCo}_2\text{O}_4$  nanoneedle arrays and accelerate electron transport for the faradic reaction due to their intrinsically excellent electrical conductivity. Second, the porous structure in the  $\text{ZnCo}_2\text{O}_4$  nanoneedle arrays could effectively facilitate electrolyte transport, enhancing the electrochemical kinetics and ensuring efficient interfacial contact between the active material and the electrolyte. Third, hierarchical PCF@ $\text{ZnCo}_2\text{O}_4$

**Table 1** The calculated values of  $R_s$ ,  $C_{dl}$ ,  $R_{ct}$ ,  $Z_w$  and  $C_L$  through CNLS fitting of the experimental impedance spectra based upon the proposed equivalent circuit in Fig. 5e

	$R_s$ ( $\Omega$ )	$C_{dl}$ (F)	$R_{ct}$ ( $\Omega$ )	$Z_w$	$C_L$ (F)
$\text{ZnCo}_2\text{O}_4$	0.227	0.0348	0.547	0.0332	0.00267
PCF@ $\text{ZnCo}_2\text{O}_4$	0.197	0.0945	0.0750	0.0262	0.00590

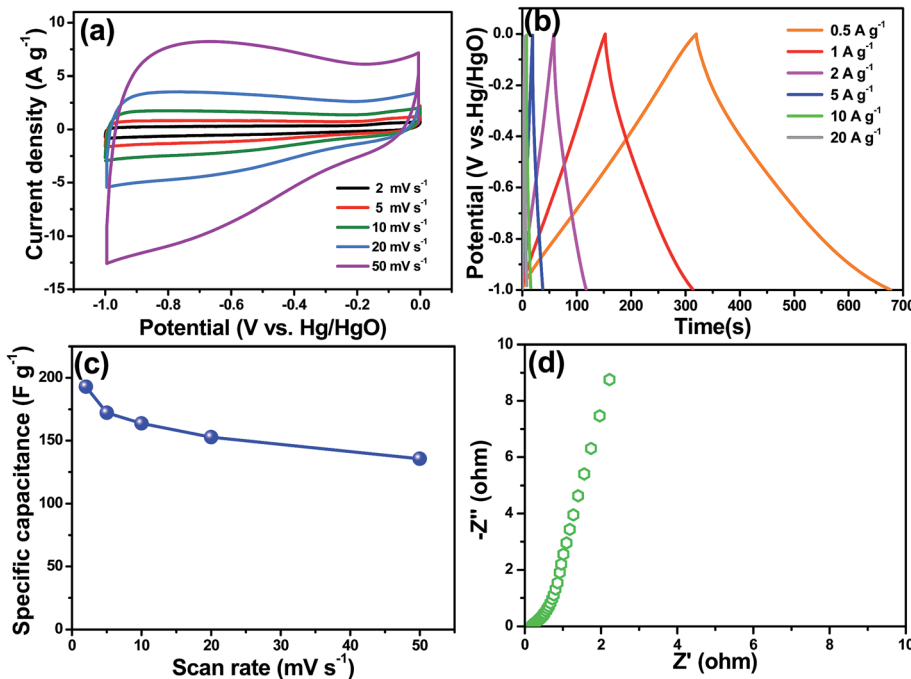


**Fig. 6** (a) CV and (b) galvanostatic charge/discharge curves of the PCF electrode at different scan rates and current densities within the potential range from  $-1$  to  $0$  V (vs.  $\text{Hg}/\text{HgO}$ ) in  $6 \text{ M KOH}$ . (c) Specific capacitance of PCF electrode at various scan rates. (d) Nyquist plot of the PCF electrode in the frequency range from 100 kHz to 0.01 Hz.

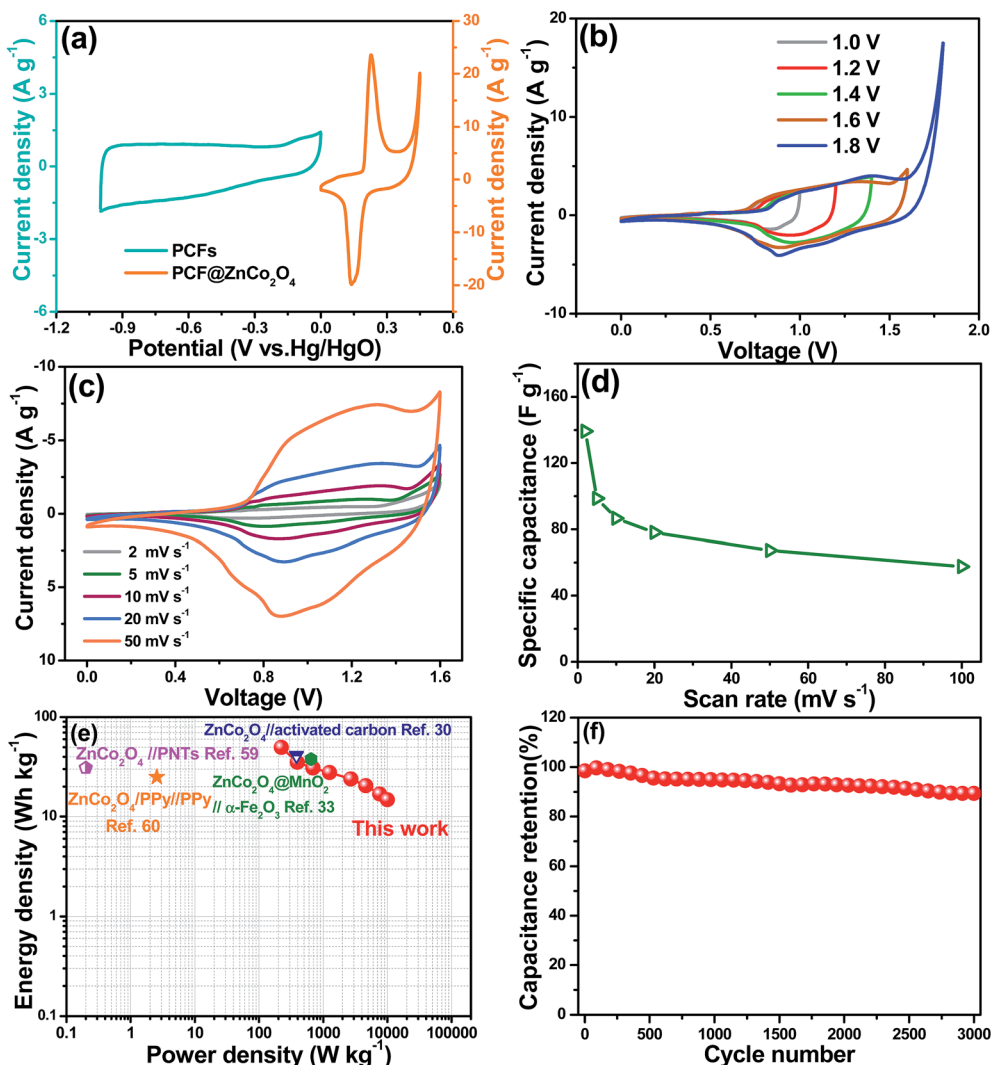


**Fig. 7** (a) CV curves of PCFs and PCF@ZnCo<sub>2</sub>O<sub>4</sub> electrodes performed in a three-electrode cell in 6 M KOH aqueous solution at a scan rate of 5 mV s<sup>-1</sup>. (b) CV curves of the PCF@ZnCo<sub>2</sub>O<sub>4</sub>//PCFs all-solid-state ASC device measured at different voltage windows with PVA/KOH polymer electrolyte. (c) CV curves of the device at various scan rates. (d) Specific capacitance as a function of scan rates. (e) Ragone plot of the PCF@ZnCo<sub>2</sub>O<sub>4</sub>//PCFs all-solid-state ASC device and the values reported previously (ZnCo<sub>2</sub>O<sub>4</sub>//MnO<sub>2</sub>/ $\alpha$ -Fe<sub>2</sub>O<sub>3</sub>,<sup>33</sup> ZnCo<sub>2</sub>O<sub>4</sub>//activated carbon,<sup>30</sup> ZnCo<sub>2</sub>O<sub>4</sub>//porous nanotubes,<sup>59</sup> and ZnCo<sub>2</sub>O<sub>4</sub>/PPy//PPy<sup>60</sup>). (f) Cycling performance of the all-solid-state ASC device measured at 50 mV s<sup>-1</sup> over 3000 cycles.

provides loose textures and open spaces between neighboring hybrid fibers, ensuring that the electrolyte ions readily penetrate into the inner region of the electrode, greatly shortening the transport/diffusion paths of electrolyte ions and increasing the utilization of the active materials. More importantly, the unique hierarchical core–shell structure could efficiently inhibit the volume changes during the charge–discharge process. Finally, the PCF@ZnCo<sub>2</sub>O<sub>4</sub> hybrid is directly used as the electrode without the use of carbon black and polymer binders, avoiding the use of “inactive” materials and improving the availability of active materials.<sup>38</sup>

### 3.3. Electrochemical characterization of PCFs

Fig. 6a shows the CV curves of PCF electrode with the scan rates from 2 to 50 mV s<sup>-1</sup> between -1 and 0 V (vs. Hg/HgO).

Obviously, all the CV curves show nearly ideal rectangular shapes without visible distortions even at a scan rate of 50 mV s<sup>-1</sup>, indicating that the PCF electrode has ideal supercapacitor behavior. Typical galvanostatic charge/discharge curves of the PCF electrode at different current densities from 0.5 to 20 A g<sup>-1</sup> are displayed in Fig. 6b. It can be seen that all of the charge and discharge curves are highly symmetric, suggesting that the electrode possesses ideal capacitive performance and splendid electrochemical reversibility. The specific capacitance of the PCF electrode, as calculated according to the CV curves, are presented in Fig. 6c. A specific capacitance of 193 F g<sup>-1</sup> is achieved at the scan rate of 2 mV s<sup>-1</sup> and remains 136 F g<sup>-1</sup> when the scan rate increases to 50 mV s<sup>-1</sup>. Fig. 6d displays the EIS analysis of the PCF electrode. As can be seen, the equivalent series resistance is 0.19 Ω, indicating a high charge and

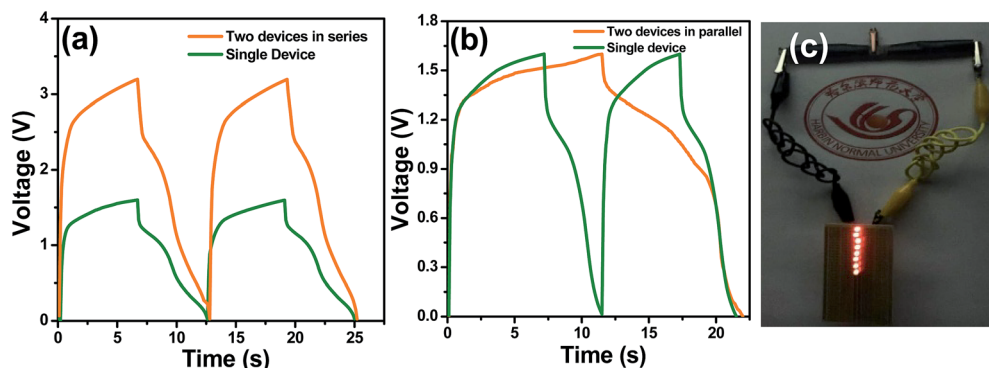


**Fig. 8** Galvanostatic charge/discharge curves of a single all-solid-state supercapacitor and two supercapacitors in (a) series and (b) parallel. (c) Two assembled all-solid-state ASC devices connected in series to simultaneously light up eight red LEDs.

discharge rate for the PCF electrode. Notably, no obvious semi-circle of the EIS plot can be observed, demonstrating fast charge transfer towards the surface of the electrode.

### 3.4. Electrochemical characterization of the all-solid-state ASC device

To further evaluate the capacitive performance of PCF@ZnCo<sub>2</sub>O<sub>4</sub> towards real applications, an all-solid-state ASC supercapacitor device was assembled using the as-prepared PCF@ZnCo<sub>2</sub>O<sub>4</sub> hybrid and PCFs as the positive and negative electrode, respectively, with PVA/KOH electrolyte and cellulose filter paper as the separator. Fig. 7a presents the corresponding voltage windows of the PCF@ZnCo<sub>2</sub>O<sub>4</sub> hybrid and PCF electrode at a scan rate of 5 mV s<sup>-1</sup>, demonstrating that they can be assembled into an ASC device due to the different potential windows. Fig. 7b shows the CV curves of the fabricated ASC at different voltage windows recorded at a scan rate of 20 mV s<sup>-1</sup>. As expected, the stable operating voltage can be extended up to 1.6 V. The CV curves of the fabricated ASC at different scan rates in the voltage window of 0–1.6 V are shown in Fig. 7c. The two broad redox peaks in each curve indicate the pseudocapacitive property of the supercapacitor due to faradic redox reactions. According to the CV curves of the ASC device, the specific capacitance based on the total mass of materials in two electrodes is calculated to be 139.2 F g<sup>-1</sup> at 2 mV s<sup>-1</sup> and remains 67.3 F g<sup>-1</sup> at 50 mV s<sup>-1</sup>, as shown in Fig. 7d. Energy and power densities are two vital parameters to characterize the electrochemical performance of supercapacitor devices. Fig. 7e shows the Ragone plot of the fabricated PCF@ZnCo<sub>2</sub>O<sub>4</sub>//PCF ASC device. The all-solid-state ASC could achieve a high energy density of 49.5 W h kg<sup>-1</sup> at a power density of 222.7 W kg<sup>-1</sup>, which is highly comparable to the previously reported ZnCo<sub>2</sub>O<sub>4</sub> based ASC devices such as ZnCo<sub>2</sub>O<sub>4</sub>@MnO<sub>2</sub>/α-Fe<sub>2</sub>O<sub>3</sub> (37.8 W h kg<sup>-1</sup>),<sup>33</sup> ZnCo<sub>2</sub>O<sub>4</sub>//activated carbon (41 W h kg<sup>-1</sup>),<sup>30</sup> ZnCo<sub>2</sub>O<sub>4</sub>//porous nanotubes (25 W h kg<sup>-1</sup>),<sup>59</sup> and ZnCo<sub>2</sub>O<sub>4</sub>/PPy//PPy (30.9 W h kg<sup>-1</sup>).<sup>60</sup>

Since the long-term cycle stability of supercapacitors is another crucial requirement in practical application, the cycling stability of the ASC device was evaluated through repeating the CV test between 0 and 1.6 V at a scan rate of 50 mV s<sup>-1</sup> for 3000

cycles (Fig. 7f). About 90% of its initial capacitance is retained after 3000 cycles, demonstrating the superior cycling stability of our fabricated ASC device. The XRD pattern and SEM image of the PCF@ZnCo<sub>2</sub>O<sub>4</sub> heterostructure after the cycling test are shown in Fig. S2.† As shown in the XRD pattern (Fig. S2a†), the diffraction peaks can be well indexed to the cubic spinel ZnCo<sub>2</sub>O<sub>4</sub> phase (JCPDS card no. 23-1390) except for those peaks ascribed to metal Ni. In addition, the hybrid still retains its initial core-shell nanostructure after the cycling tests (Fig. S2b†), suggesting a stable structure for the PCF@ZnCo<sub>2</sub>O<sub>4</sub>.

It is generally accepted that the total energy stored in a single cell can not satisfy the power and energy requirements for most practical applications. Thus, in order to form a reasonable specific voltage and capacitance rating for some practical microelectronic applications, supercapacitors need to be connected together in series or parallel combinations.<sup>61,62</sup> Fig. 8a exhibits the galvanostatic charge/discharge curves of a single device and two devices connected in series. The operating voltage window of the series (3.2 V) is widened to double that of the single device. Fig. 8b shows the galvanostatic charge/discharge curves of the two connected in parallel. Compared to a single device, the overall capacitance is two times by a factor of two under the same voltage window of 0 to 1.6 V. The discharge time is about two times longer than that of a single device, which also attests to the good capacitive performance in parallel assembly. To highlight its potential application, our fabricated all-solid-state ASC was used to light a commercial red light-emitting diode (LED). Impressively, the two all-solid-state ASC devices connected in series are capable of simultaneously lighting up eight red LEDs after being charged to 3.2 V (Fig. 8c), demonstrating the excellent practical application potentials of the devices as an energy storage system.

## 4. Conclusions

In summary, the hierarchical PCF@ZnCo<sub>2</sub>O<sub>4</sub> nanoneedle has been successfully synthesized. The as-obtained PCF@ZnCo<sub>2</sub>O<sub>4</sub> electrode exhibits a high specific capacitance of 1384 F g<sup>-1</sup> at a scan rate of 2 mV s<sup>-1</sup>. In addition, an all-solid-state ASC device based on PCF@ZnCo<sub>2</sub>O<sub>4</sub> and PCFs is well designed. The fabricated and optimized ASC device exhibits a high energy density

of  $49.5 \text{ W h kg}^{-1}$ , which is highly comparable to the previously reported  $\text{ZnCo}_2\text{O}_4$  based ASC systems and has superior cycling stability (90% capacitance retention after 3000 cycles). Moreover, an application of our high-performance ASC device has been demonstrated by switching red LEDs, endowing our all-solid-state ASC new opportunities as energy storage devices for various portable electronic systems.

## Acknowledgements

The authors acknowledge the financial support from the National Natural Science Foundation of China (21471041, 21171045), the Natural Science Foundation of Heilongjiang Province of China (ZD201214), and the Technology Development Pre-project of Harbin Normal University (12XYG-11).

## References

- J. Xiao, L. Wan, S. Yang, F. Xiao and S. Wang, *Nano Lett.*, 2014, **14**, 831–838.
- G. Zhang and X. W. Lou, *Adv. Mater.*, 2013, **25**, 976–979.
- Q. Yang, Z. Lu, X. Sun and J. Liu, *Sci. Rep.*, 2013, **3**, 3537.
- Q. Zhang, M. Q. Zhao, D. M. Tang, F. Li, J. Q. Huang, B. Liu, W. C. Zhu, Y. H. Zhang and F. Wei, *Angew. Chem., Int. Ed.*, 2010, **49**, 3642–3645.
- J. Qu, L. Shi, C. He, F. Gao, B. Li, Q. Zhou, H. Hu, G. Shao, X. Wang and J. Qiu, *Carbon*, 2014, **66**, 485–492.
- T. Zhai, F. Wang, M. Yu, S. Xie, C. Liang, C. Li, F. Xiao, R. Tang, Q. Wu, X. Lu and Y. Tong, *Nanoscale*, 2013, **5**, 6790–6796.
- J. Yan, Q. Wang, C. Lin, T. Wei and Z. Fan, *Adv. Energy Mater.*, 2014, **4**, 1400500.
- S. Feng, W. Li, J. Wang, Y. Song, A. A. Elzatahry, Y. Xia and D. Zhao, *Nanoscale*, 2014, **6**, 14657–14661.
- H. Niu, D. Zhou, X. Yang, X. Li, Q. Wang and F. Qu, *J. Mater. Chem. A*, 2015, **3**, 18413–18421.
- C. Zhang, H. Yin, M. Han, Z. Dai, H. Pang, Y. Zheng, Y.-Q. Lan, J. Bao and J. Zhu, *ACS Nano*, 2014, **8**, 3761–3770.
- X. Zhao, Q. Zhang, C.-M. Chen, B. Zhang, S. Reiche, A. Wang, T. Zhang, R. Schlögl and D.-S. Su, *Nano Energy*, 2012, **1**, 624–630.
- S. Gao, Y. Sun, F. Lei, L. Liang, J. Liu, W. Bi, B. Pan and Y. Xie, *Angew. Chem., Int. Ed.*, 2014, **53**, 12789–12793.
- C.-M. Chen, Q. Zhang, M.-G. Yang, C.-H. Huang, Y.-G. Yang and M.-Z. Wang, *Carbon*, 2012, **50**, 3572–3584.
- Y.-Z. Liu, C.-M. Chen, Y.-F. Li, X.-M. Li, Q.-Q. Kong and M.-Z. Wang, *J. Mater. Chem. A*, 2014, **2**, 5730–5737.
- W. Lv, D.-M. Tang, Y.-B. He, C.-H. You, Z.-Q. Shi, X.-C. Chen, C.-M. Chen, P.-X. Hou, C. Liu and Q.-H. Yang, *ACS Nano*, 2009, **3**, 3730–3736.
- Y. Zhu, C. Cao, S. Tao, W. Chu, Z. Wu and Y. Li, *Sci. Rep.*, 2014, **4**, 5787.
- Y. Z. Zhang, J. Zhao, J. Xia, L. Wang, W. Y. Lai, H. Pang and W. Huang, *Sci. Rep.*, 2015, **5**, 8536.
- M. Huang, Y. Zhang, F. Li, Z. Wang, Alamusni, N. Hu, Z. Wen and Q. Liu, *Sci. Rep.*, 2014, **4**, 4518.
- J. Zhao, J. Chen, S. Xu, M. Shao, Q. Zhang, F. Wei, J. Ma, M. Wei, D. G. Evans and X. Duan, *Adv. Funct. Mater.*, 2014, **24**, 2938–2946.
- J. Yan, Q. Wang, T. Wei and Z. Fan, *Adv. Energy Mater.*, 2014, **4**, 1300816.
- H. Wang, H. S. Casalongue, Y. Liang and H. Dai, *J. Am. Chem. Soc.*, 2010, **132**, 7472–7477.
- P. Yang, Y. Ding, Z. Lin, Z. Chen, Y. Li, P. Qiang, M. Ebrahimi, W. Mai, C. P. Wong and Z. L. Wang, *Nano Lett.*, 2014, **14**, 731–736.
- D. Zhou, H. Lin, F. Zhang, H. Niu, L. Cui, Q. Wang and F. Qu, *Electrochim. Acta*, 2015, **161**, 427–435.
- X. Zhang, Y. Zhao and C. Xu, *Nanoscale*, 2014, **6**, 3638–3646.
- S. Hou, G. Zhang, W. Zeng, J. Zhu, F. Gong, F. Li and H. Duan, *ACS Appl. Mater. Interfaces*, 2014, **6**, 13564–13570.
- H.-P. Cong, X.-C. Ren, P. Wang and S.-H. Yu, *Energy Environ. Sci.*, 2013, **6**, 1185–1191.
- F. Liu, G. Han, Y. Chang, D. Fu, Y. Li and M. Li, *J. Appl. Polym. Sci.*, 2014, **131**, 39779.
- Y. Chen, M. Han, Y. Tang, J. Bao, S. Li, Y. Lan and Z. Dai, *Chem. Commun.*, 2015, **51**, 12377–12380.
- H. Chen, L. Hu, M. Chen, Y. Yan and L. Wu, *Adv. Funct. Mater.*, 2014, **24**, 934–942.
- B. Guan, D. Guo, L. Hu, G. Zhang, T. Fu, W. Ren, J. Li and Q. Li, *J. Mater. Chem. A*, 2014, **2**, 16116–16123.
- H. Hu, B. Guan, B. Xia and X. W. Lou, *J. Am. Chem. Soc.*, 2015, **137**, 5590–5595.
- Y. Xu, X. Wang, C. An, Y. Wang, L. Jiao and H. Yuan, *J. Mater. Chem. A*, 2014, **2**, 16480–16488.
- W. Ma, H. Nan, Z. Gu, B. Geng and X. Zhang, *J. Mater. Chem. A*, 2015, **3**, 5442–5448.
- K.-Y. Chun and I. K. Moon, *RSC Adv.*, 2015, **5**, 807–811.
- B. Liu, B. Liu, Q. Wang, X. Wang, Q. Xiang, D. Chen and G. Shen, *ACS Appl. Mater. Interfaces*, 2013, **5**, 10011–10017.
- B. Guan, D. Guo, L. Hu, G. Zhang, T. Fu, W. Ren, J. Li and Q. Li, *J. Mater. Chem. A*, 2014, **2**, 16116–16123.
- S. Wang, J. Pu, Y. Tong, Y. Cheng, Y. Gao and Z. Wang, *J. Mater. Chem. A*, 2014, **2**, 5434–5440.
- Q. Wang, L. Zhu, L. Sun, Y. Liu and L. Jiao, *J. Mater. Chem. A*, 2015, **3**, 982–985.
- J. Cheng, Y. Lu, K. Qiu, H. Yan, X. Hou, J. Xu, L. Han, X. Liu, J.-K. Kim and Y. Luo, *Phys. Chem. Chem. Phys.*, 2015, **17**, 17016–17022.
- K. Qiu, Y. Lu, D. Zhang, J. Cheng, H. Yan, J. Xu, X. Liu, J.-K. Kim and Y. Luo, *Nano Energy*, 2015, **11**, 687–696.
- X. Lu, M. Yu, G. Wang, T. Zhai, S. Xie, Y. Ling, Y. Tong and Y. Li, *Adv. Mater.*, 2013, **25**, 267–272.
- L. Bao, J. Zang and X. Li, *Nano Lett.*, 2011, **11**, 1215–1220.
- Y. Dong, H. Lin, D. Zhou, H. Niu, Q. Jin and F. Qu, *Electrochim. Acta*, 2015, **159**, 116–123.
- D. Zhou, Y. Dong, L. Cui, H. Lin and F. Qu, *J. Nanopart. Res.*, 2014, **16**, 1–9.
- W. Li, F. Zhang, Y. Dou, Z. Wu, H. Liu, X. Qian, D. Gu, Y. Xia, B. Tu and D. Zhao, *Adv. Energy Mater.*, 2011, **1**, 382–386.
- X. Yang, F. Qu, H. Niu, Q. Wang, J. Yan and Z. Fan, *Electrochim. Acta*, 2015, **180**, 287–294.

- 47 B. Liu, J. Zhang, X. Wang, G. Chen, D. Chen, C. Zhou and G. Shen, *Nano Lett.*, 2012, **12**, 3005–3011.
- 48 R. Madhu, V. Veeramani, S.-M. Chen, P. Veerakumar and S.-B. Liu, *Chem.-Eur. J.*, 2015, **21**, 8200–8206.
- 49 F. Bao, X. Wang, X. Zhao, Y. Wang, Y. Ji, H. Zhang and X. Liu, *RSC Adv.*, 2014, **4**, 2393–2397.
- 50 C. Yuan, J. Li, L. Hou, X. Zhang, L. Shen and X. W. D. Lou, *Adv. Funct. Mater.*, 2012, **22**, 4592–4597.
- 51 W. Hu, R. Chen, W. Xie, L. Zou, N. Qin and D. Bao, *ACS Appl. Mater. Interfaces*, 2014, **6**, 19318–19326.
- 52 D. Kong, J. Luo, Y. Wang, W. Ren, T. Yu, Y. Luo, Y. Yang and C. Cheng, *Adv. Funct. Mater.*, 2014, **24**, 3815–3826.
- 53 Z. Wu, X. L. Huang, Z. L. Wang, J. J. Xu, H. G. Wang and X. B. Zhang, *Sci. Rep.*, 2014, **4**, 3669.
- 54 G. Zhang and X. W. David Lou, *Sci. Rep.*, 2013, **3**, 1470.
- 55 Q. Wang, J. Du, Y. Zhu, J. Yang, J. Chen, C. Wang, L. Li and L. Jiao, *J. Power Sources*, 2015, **284**, 138–145.
- 56 L. C. Wu, Y. J. Chen, M. L. Mao, Q. H. Li and M. Zhang, *ACS Appl. Mater. Interfaces*, 2014, **6**, 5168–5174.
- 57 J. Yan, W. Sun, T. Wei, Q. Zhang, Z. Fan and F. Wei, *J. Mater. Chem.*, 2012, **22**, 11494.
- 58 D. Cheng, Y. Yang, J. Xie, C. Fang, G. Zhang and J. Xiong, *J. Mater. Chem. A*, 2015, **3**, 14348–14357.
- 59 G. Zhou, J. Zhu, Y. Chen, L. Mei, X. Duan, G. Zhang, L. Chen, T. Wang and B. Lu, *Electrochim. Acta*, 2014, **123**, 450–455.
- 60 T. Chen, Y. Fan, G. Wang, Q. Yang and R. Yang, *RSC Adv.*, 2015, **5**, 74523–74530.
- 61 M. F. El-Kady and R. B. Kaner, *Nat. Commun.*, 2013, **4**, 1475.
- 62 H. Jin, L. Zhou, C. L. Mak, H. Huang, W. M. Tang and H. L. Wa Chan, *J. Mater. Chem. A*, 2015, **3**, 15633–15641.